Marine Sediment Characterized by Ocean-Bottom Fiber-Optic Seismology

Zack J. Spica[1,†], Kiwamu Nishida[2], Takeshi Akuhara[2], François Pétrélis[3,†], Masanao Shinohara[2], Tomoaki Yamada[4,†]

[1]Department of Earth and Environmental Sciences, University of Michigan, Ann Arbor, Michigan, U.S.A.
[2]Earthquake Research Institute, The University of Tokyo, Tokyo, Japan
[3]Laboratoire de Physique de l'École normale supérieure, ENS, Université PSL, CNRS, Sorbonne Université, Université Paris-Diderot, Sorbonne Paris Cité, Paris, France
[4]Japan Meteorological Agency, Tokyo, Japan
[†]Formerly at Earthquake Research Institute, The University of Tokyo, Tokyo, Japan

Key Points:

- Ocean-bottom Distributed Acoustic Sensing is used to image shallow V_S structure.
- Rayleigh wave phase velocity dispersion curves are extracted from frequency-wavenumber analysis.
- Reflection image is obtained from auto-correlations of ambient seismic field.

Corresponding author: Zack J. Spica, zspica@umich.edu

Abstract

The Sanriku ocean-bottom seismometer system uses an optical fiber cable to guarantee real-time observations at the seafloor. A dark fiber connected to a Distributed Acoustic Sensing (DAS) interrogator converted the cable in an array of 19,000 seismic sensors. We use these measurements to constrain the velocity structure under a section of the cable. Our analysis relies on 24h of ambient seismic field recordings. We obtain a high-resolution 2D shear-wave velocity profile by inverting multi-mode dispersion curves extracted from frequency-wavenumber analysis. We also produce a reflection image from auto-correlations of ambient seismic field, highlighting strong impedance contrasts at the interface between the sedimentary layers and the basement. In addition, earthquake wavefield analysis and modeling, help to further constrain the sediment properties under the cable. Our results show for the first time that ocean-bottom DAS can produce detailed images of the subsurface, opening new opportunities for cost-effective ocean-bottom imaging in the future.

Plain Language Summary

Distributed Acoustic Sensing (DAS) is a relatively new measurement method that has the potential to convert existing fiber optic communication infrastructure into arrays of thousands of seismic sensors. In this research, we connected a DAS to a cable that was originally installed at the bottom of the ocean to sustain a seismic and tsunami observatory in the Sanriku region. We show that this new type of measurement can provide reliable information to image and explore the shallow subsurface under this fiber cable. This is the first time such analysis is performed in an oceanic environment, and our methods could be readily exportable to other fiber-optic cables that are the backbones of our modern telecommunication.

1 Introduction

The accurate determination of models of the shear velocity of marine sediments has significant implication for many different fields both in academia and industry. For geotechnical applications, such as the construction of offshore platforms and pipelines, these models provide constraints on the shear modulus (Ayres and Theilen, 2001) and allow quantifying sediment stability and earthquake amplification effects (Sanchez-Sesma, 1987; Akal and Berkson, 2013). For seismic imaging, shear-waves velocity models are required to improve the processing algorithms for multicomponent seismic data like static correction for converted PS-waves (e.g., Muyzert, 2000), wavefield separation (e.g., Schalkwijk et al., 2000) or other imaging techniques with phase conversion (e.g., Akuhara et al., 2019). Also, combination of both S- and P-wave velocities helps to better interpret the lithology because together they are much more sensitive to fluid and gas contents than P-wave alone (Ayres and Theilen, 2001).

Other than direct core sampling, our knowledge of the shear-wave properties of the sediments is largely based on active and passive seismic surveys (e.g., Socco et al., 2011; Mordret et al., 2013). With active seismic, measurements of sediment shear-wave speed are problematic because active sources in water require strong energy conversion to produce significant body shear wave on seafloor. As a result, simple evaluation of the shear-wave structure lags far behind the detailed 3D mapping techniques existing for P-wave (e.g., Vardy et al., 2017). Therefore, both active and passive methods generally promote the use of the low-frequency solid-liquid interface waves (a.k.a Scholte waves (Scholte, 1958; Nolet and Dorman, 1996)) to constrain the shear-wave structure in water (e.g., Kugler et al., 2007; Ritzwoller and Levshin, 2002). These surface waves can be retrieved from active P-wave seismic records but are also naturally and permanently generated by the ocean mass movements. Indeed, the interactions of surface gravity waves are at the origin of the secondary microseism (e.g., Longuet-Higgins, 1950; Hasselmann, 1963; Ardhuin et al., 2011), which is the main seismic source used in offshore ambient seismic field (ASF) correlation studies (e.g., Yao et al., 2011; Mordret et al., 2014).

Although these methods may provide high resolution, they are usually limited in extent (e.g., Kugler et al., 2007; Mordret et al., 2013). The development of large-scale seismic experiments involving the deployment of multiple ocean bottom seismographs (e.g., Kanazawa et al., 2016) has offered the opportunity to constrain sediment thickness over larger areas but at the cost of a much lower resolution. In addition, certain of these seismic networks are restricted in time (from a few months to a ∼year), limiting their potential for continuous monitoring (e.g., Shinohara et al., 2012). An appealing alternative is the emerging technology of Distributed Acoustic Sensing (DAS) that turns fiber-optic cables into thousands of seismic sensors (Grattan and Sun, 2000; Posey Jr. et al., 2000). The fiber is probed by repeated laser pulses and an interferometer analyzes the backscattered light to measure the deformation (strain) along the fiber due to its interaction with seismic waves. The obtained waveforms at each channel are then not point measurements but rather are strains measured over a spatial distance (the gauge length) in the direction of the cable. As the fiber is a passive component, no extra electronic device is needed and the fiber may be left on the ocean floor for a virtually unlimited amount of time. The fiber offers real-time telemetry for thousands of synchronized sensors and works on one single power source. Furthermore, fiber cables abound in certain oceanic regions as they are the backbone of telecommunication networks. Lately, ocean-bottom DAS prototype experiments have shown promises to monitor the ocean-solid earth interactions and to detect oceanic seismicity with signal characteristics comparable to those of ocean-bottom seismometers (OBS) (Lindsey et al., 2019; Shinohara et al., 2019; Sladen et al., 2019; Williams et al., 2019).

In this communication, we demonstrate for the first time that DAS can be used to passively image shallow sediments at the bottom of the ocean. Our analysis relies only on one day of ASF recorded with a fiber cable originally installed for telecommunication between OBS systems in the Sanriku region, Japan (Fig. 1). ASF is used to extract multi-mode Rayleigh wave dispersion curves that we invert locally to provide a 2D shear-wave velocity profile under a section of the cable with a resolution and an extent that would be hard to obtain with traditional OBS or hydrophone arrays. In addition, auto-correlations of ASF computed for the first ∼10,000 channels of the array deliver a reflection image of the shallow sedimentary layers. This image sheds light on strong impedance contrast and possible sharp amplification of seismic waves in a particular region of the continental slope in connection with extremely low velocity sediments. Our approaches do not require costly off-shore dedicated survey, can be repeated at different times at almost no additional cost and could be readily exported to other existing ocean-bottom fiber cables worldwide to provide high-resolution structural images of the ocean-bottom seismic properties.

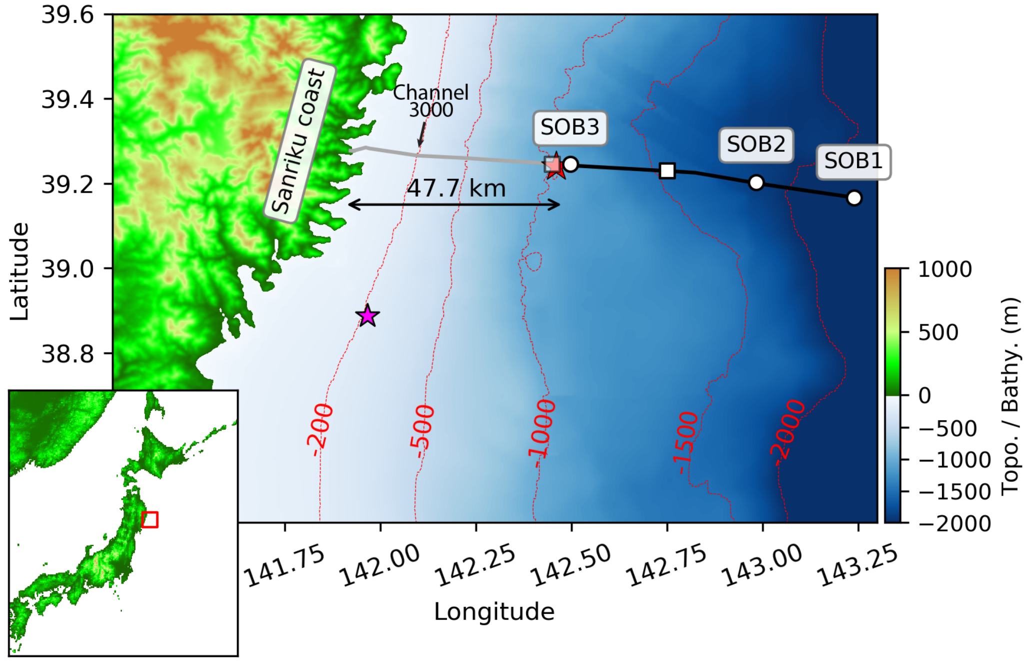

Figure 1: Map showing the location of the telecommunication fiber-optic cable off the shore of Sanriku. The grey section of the cable, which is used in our analyses, is buried under 60-70 cm of sediment while the black section lies directly on the seafloor by gravity. The white dots depict the accelerometers and the white squares are the pressure gauges. The pink star depicts the location of an earthquake (2019-02-14T21:10:50; M_w=3.0) recorded by DAS and shown in Fig. 3C. The red star depicts the location of another earthquake recorded only by the OBS systems (2018-01-30T17:20:56.31; M_w=3.1; depth=30.9 km) and showed in Fig. 4.

2 Materials & Methods

2.1 The Sanriku fiber cable

DAS is particularly cost-effective if a pre-installed fiber-optic cable is available. Here, we take advantage of one submarine telecommunication cable system (Fig. 1) that was installed in 1996 to sustain an ocean-bottom seismic observatory (Kanazawa and Hasegawa, 1997) located near the source area of the 2011 Tohoku-oki earthquake (e.g., Suzuki et al., 2011). The system is composed of a 120 km cable with three 3-component accelerometers and two pressure gauges. Although the great Tohoku-oki earthquake damaged the landing station, the cable system was restored in 2014 (Shinohara et al., 2016). According to the installation report, the cable is buried 0.6-0.7 m below the seafloor from the coast until the point where the water column reaches 997 m (i.e., ∼47.7 km from the landing station). A DAS interrogator unit with a 100-km sensing range (AP Sensing N5200A; Cedilnik et al. (2019)) was connected to the landing end of the fiber and data were acquired at 500 Hz for about 46 h starting on February 13th, 2019. The gauge length was initially set to 10 m but it was changed to 40 m after about 90 minutes of recordings. The spacial sampling was set to 5 m, yielding to an array of ∼19,000 horizontal channels along the 100 first kilometers of the cable. In this contribution, we use the 40 m gauge length, and only analyze the first ∼48 km, which corresponds to the buried section of the cable where we can guarantee a better coupling between the cable and the seafloor. Both the DAS and the OBS system were operational during the experiment. More details about the cable setup and measurement quality can be found in Shinohara et al. (2019).

2.2 2D shear-wave velocity profile

2.2.1 Phase velocity from frequency-wavenumber analysis

Applying a 2D Fourier transform to a 2h strain record of a group of channels allows identification and separation of coherent oceanic and seismic signals in the frequency-wavenumber (FK) domain. Figs. 2 and S1 show the FK power spectrum for a subset of 1000 channels centered on channel # 3000 and 8000, respectively. Given the linear geometry of the cable, the observed signals can be easily interpreted for both incoming (landward) and reflected energies. Such spectral analysis can also be repeated along the length of the buried cable with a moving window of 500 channels to evaluate the fluctuations of the wave energies as a function of distance from the coast or depth (Fig. 3a).

Ocean surface gravity waves appear at frequencies lower than ∼0.2 Hz near the coast and with peak frequency under 0.12 Hz off the coast (Figs. 2, 3a). In Fig 2c", they show an apparent phase velocity of ∼40 m/s, when projected in the frequency-phase velocity space. Their attenuation with depth and their dispersion follow the linear gravity wave theory ($\omega^2 = gk \tanh(kH)$; e.g., Gill (1982)), meaning that these coherent seismic energies represent the generation of primary microseisms in-situ (e.g., Williams et al., 2019). Although of interest, the detailed analysis of these surface gravity waves propagating across the array is out of the scope of this contribution.

When surface gravity waves interfere non-linearly with nearly opposite wave numbers, they generate a double-frequency pressure fluctuation that can propagate efficiently in the deep waters until and through the seabed (e.g., Longuet-Higgins, 1950; Hasselmann, 1963; Ardhuin et al., 2011). This phenomenon is at the origin of the secondary microseisms and is well observed in our data at depths greater than ∼150 m (Fig. 3a). Figs. 2c and S1c show distinct dispersive wave packets with dominant frequencies at ∼0.75 and ∼0.5 Hz, respectively. Both show phase velocities ranging from ∼300-600 m/s to ∼1500 m/s, suggesting that they are seismo-acoustic surface waves controlled by the properties of the shallow sediments and the speed of acoustic waves in water (Williams et al., 2019). These dispersive waves are most likely Scholte waves as the fiber-optic DAS is more sensitive to longitudinally propagating waves than horizontally polarized waves with motion almost perpendicular to the cable (i.e., Love waves).

Numerical calculation of dispersion curves (Herrmann, 1996) for a known velocity model of the region (Fig. S2) further suggests this hypothesis as it approximates fairly well the fundamental and higher modes observed in Fig. S1c (black lines). In the region, the P wave velocity (Vp) of the Neogene marine sediment is ∼2400 m/s (Kodaira et al., 2017) and S wave velocity (Vs) can be approximated to ∼600 m/s using a Vp/Vs of ∼4 (Nakamura et al., 2014). The thickness has been reported as 1200–1800 m (Kodaira et al., 2017). The Vp and Vs of the Cretaceous basement near its top is ∼4.7-5.5 and ∼2.4-2.7 km/s, respectively (Shinohara et al., 2008; Kodaira et al., 2017). The densities of the sediments and the basement in the northwest Pacific is reported as ∼1.350 g/cm^3 and 2.750 g/cm^3, respectively (Kanazawa et al., 2001). On the other hand, to approximate the higher frequency dispersive signal at channel #3000 (Fig. 2c, black line), a much lower velocity (Vs = 300), a thinner sediment layer, and a Vp/Vs ratio of 8 (e.g., Nakamura et al., 2014) are needed. The velocity models used in this analysis are shown in Fig. S2.

We extracted these phase velocity dispersion curves by selecting the local maxima in a given region of the FK power spectrum. This process was performed using a graphical user interface that involves visual validation of the dispersion curves (e.g., Spica et al., 2015). Validation is guided through theoretical dispersion curves for estimated velocity models of the region, as describe above. This process was performed for 45 locations along the cable (each ∼1000 m). When present in the data, both fundamental and higher modes were extracted. The error on the picking is intrinsic to the size of the bin in which the maximum is selected. This leads to a much larger error at higher velocities (Fig. 2c).

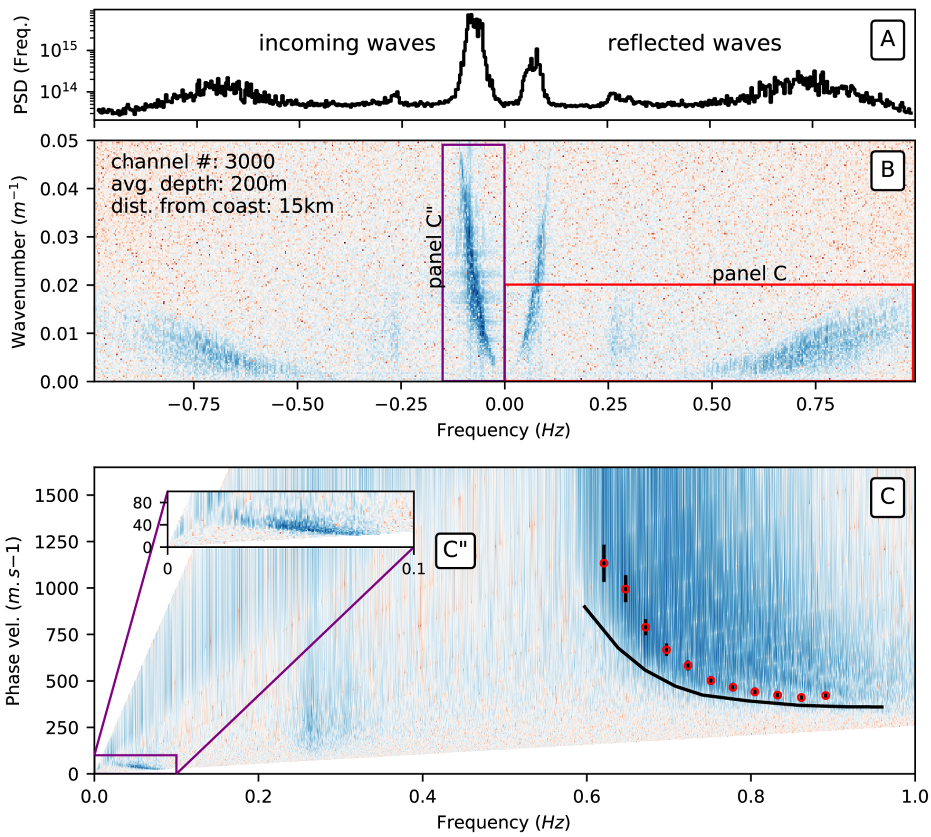

Figure 2: A) Power Spectral Density of panel B. B) FK power spectrum of a subset of 1000 channels centered on channel #3000. The colored boxes highlight the region used to compute panel C and C". C) Same as the red region in B but after conversion to the phase velocity frequency domain. Black line depicts the fundamental mode of the Scholte waves for a suggested velocity model shown in Fig. S2. Red dots with error bars are the extracted phase velocity used for inversion. C") Same as the purple region in B but after conversion to the phase velocity frequency domain and where we observe the dispersion of the ocean gravity waves.

2.2.2 Inversion for shallow shear-wave estimates

The dispersion curves were resampled using a polynomial function and then inverted using a simulated annealing algorithm that minimizes the misfit value calculated as the semblance between the data and the synthetics. Then, the inversion algorithm switched to nonlinear optimization procedure (gradient method) to reach the global minimum faster (e.g., Perton et al., 2017). The inversion was performed for thickness and S-wave velocity for two layers overlying a half-space. The first initial velocity model was constrained based on our previous estimation of the velocity model (section 2.2.1) and then, the initial velocity model in the inversion was taken as the last output model of the previously inverted velocity model, providing a natural smoothing for the entire 2D model. Examples of 1-D S-wave velocity models for selected channels are shown in Fig. S3 and the complete 2D velocity profile is shown in Fig. 3b.

Overall, the agreement between synthetics and observations is very good; however, we observe a light deterioration of this agreement at higher frequency near channel #3000. In this area of the cable, inverted velocities of the topmost layers appear to be as low as ∼300 m/s, suggesting an extreme impedance contrast with the basement layers which displays an average shear-wave velocity of ∼2100 m/s. Elsewhere, we observe an average velocity of ∼500-700 m/s for the shallow layers. From the west to the east of the cable, the sedimentary layer tends to get thicker.

2.3 Reflection image from auto-correlations

Based on an extensive theoretical and experimental work, the 1D Green's function stems from averaging auto-correlation of recorded motions (e.g., Claerbout, 1968). Several studies have shown that these zero-offset correlations can be used to constrain the local structure beneath a seismic station (e.g., Ruigrok and Wapenaar, 2012; Tonegawa et al., 2013; Kennett et al., 2015; Oren and Nowack, 2016; Sun and Kennett, 2016; Taylor et al., 2016; Phạm and Tkalčić, 2017; Saygin et al., 2017; Spica et al., 2017; Romero and Schimmel, 2018; Buffoni et al., 2019; Clayton, 2020); however because the ASF is generally dominated by surface waves, sub-critical body wave reflections are somehow more challenging to extract. In addition, the convolution of a delta pulse at zero time lag with the effective noise source time function generates wide zero-lag sidelobes that sometimes hide the shallow subsurface reflections (Romero and Schimmel, 2018). Therefore, adapted processing, such as frequency filtering and source deconvolution must be carefully applied, and this processing may vary from one dataset to another.

After downsampling the records to 25 Hz and removing major earthquakes, the auto-correlations were computed for each channel using 24h of ASF signal and with a moving window of 30 s with 50% overlap. We applied the phase-weighted stacking method to stack each window (Schimmel and Paulssen, 1997). Then, each individual auto-correlation is deconvolved by a source term computed as the moving average auto-correlation over 500 channels, centered on the selected channel. The removal of the source function allows revealing better variations in the lateral structure. The different steps of this procedure are illustrated in Fig. S4 and the final image filtered between 0.8-4.5 Hz is shown in Fig. 3c.

Fig. 3c displays distinctive features between the western and eastern section of the cable. From channels ∼2,500 to ∼5,000 a coherent but complex reflection pattern is drawn by the auto-correlation functions. After channel ∼5,500, we observe a double reflection with opposite polarity at ∼4.9 and ∼9.8 s (yellow features in Fig. 3c). The amplitude of the first reflection is much higher than the second one, and both of them are intermittently weakened in certain regions. Between channels 500 to ∼1,000 we observe another double reflection with much higher amplitude. As a whole, the reflection profile shows strong lateral variation, suggesting the presence of different volumetric heterogeneities under the cable.

3 Discussion

The wave propagation characteristics retrieved from ASF auto-correlations are closely related to the proportion of the different waves existing in the records but also on the frequency band and the component used as well as the geological structure under the cable. Here, we used a frequency band of 0.8-4.5 Hz, which is not expected to be contaminated by anthropological noise at the bottom of the ocean. Under 1 Hz, the signal is largely dominated by surface wave energy (Figs. 2, 3a) while at higher frequency we may expect more body wave contribution (e.g., Saygin et al., 2017). DAS channels are parallel to the cable axis (i.e., mostly horizontal), and as the DAS is primarily sensitive to waves traveling longitudinally along the cable (Martin et al., 2018), the extracted auto-correlation signals are most likely surface waves or body waves with motion parallel to

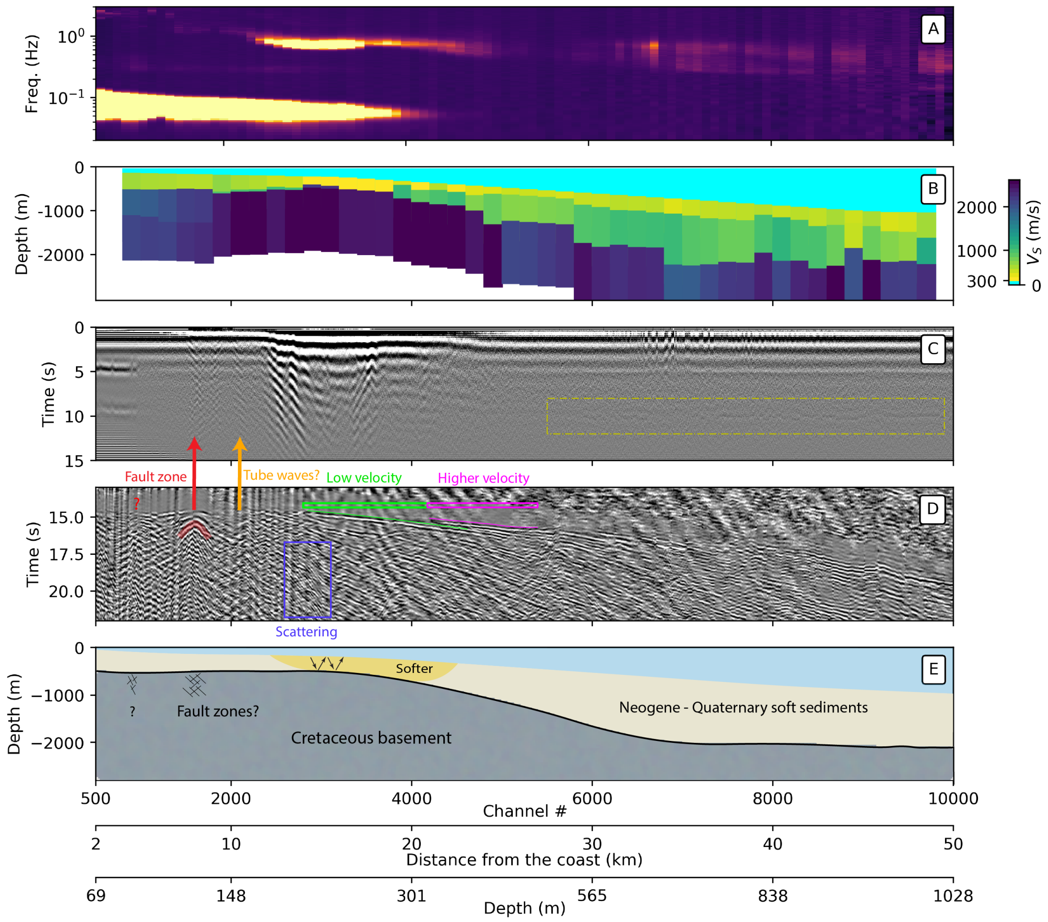

Figure 3: A) Power spectral densities along the cable every 500 channel, as shown in Fig. 2a (oceanward). B) 2D shear-wave velocity profile obtained from the inversion of the dispersion curves at each subset of 1,000 channels, as shown in Fig. S3. C) Reflection image from auto-correlations of ASF. All auto-correlation functions are bandpass filtered between 0.8-4.5 Hz. The yellow box highlights potential velocity contrast corresponding to a four-way travel times reflected S waves. A zoom in the yellow box is shown in Fig. S4d. D) S-wave arrivals with automatic gain control for an earthquake recorded by the array as shown in Fig. 1. In the green area the S wave arrives after the S wave in the purple area, which suggests a lower velocity zone. The inverted V shapes, that may characterize fault zones, are highlighted with a red arrow and a red question mark. These fault-zone regions are sometimes associated with amplification effects observed in the auto-correlation functions. Other amplification or scattering effects (orange arrow and blue box) may also be explained by localized tube waves or basin-edge scattering. E) Geological interpretation that combines the observations of all panels.

the cable (Rayleigh or S waves) (e.g., Miyazawa et al., 2008; Tonegawa et al., 2013; Spica et al., 2017).

The most striking feature of the reflection image is observed from channel ~1,200 to ~5,000. Here, a strong coherent wavefield is drawn by the auto-correlation functions and no sharp travel time is identifiable. This coherent wavefield appears where we observe the highest Scholte wave energy along the cable (Fig 3a). In this area of the cable, the inverted velocity profile indicates extreme low shear-wave velocities (~300 m/s) for a thin sedimentary layer. Therefore, we hypothesize that the strong impedance contrast existing between the bedrock and the sedimentary layer promotes multiple reverberation and trapping of the surface waves in a low velocity micro basin resulting in the reverberating pattern observed in this section of the cable (Fig 3e). Since sedimentary basin trapped waves arise from constructive interference of multiple reflections at the boundaries between the low-velocity sediments and high velocity surrounding rocks, the features of trapped waves (including amplitudes and frequency contents) are strongly dependent on the basin geometry and physical properties. By combining the methods described here, we could therefore further resolve the geometry and seismic properties of a small low velocity basin from tens to several hundreds of meters using the DAS records.

Fig. 3d depicts the wavefield after the S-wave arrival for a local M_w=3 earthquake (Fig. 1). Here, the S-wave front arrives later in the green region (low-velocity) than in the purple region (higher velocity), which further suggests the presence of a small low velocity basin. To exemplify this connection, we computed a set of 2D finite-difference seismograms (Li et al., 2014) with similar source parameter than the earthquake in Fig. 3c (see Tab. T1). They are calculated with a two-domain (i.e., fluid and solid) velocity model that includes realistic bathymetry with different levels of smoothness along the fiber-optic cable (Koketsu et al., 2012), and to which we added a shallow, thin low-velocity layer (Fig. S5a). The synthetic waveforms (Fig. S5b) show a systematic delay in the low velocity region, but also the occurrence of strong basin-edge scattering.

Under the red arrow in Fig. 3d, we observe coherent seismic energy propagating outward and showing apparent velocity of 400 to 600 m/s. This inverted v-shape feature is characteristic of waveguide effects where seismic energy interacts with highly fractured medium or low-velocity fault zones (e.g., Lindsey et al., 2019). Interestingly, this effect is also visible in the reflection image (top of the red array in Fig. 3c) suggesting strong reverberation of the ASF in a sub-vertical fault. However, similar features in the auto-correlations are not always associated with clear fault zones attributes in the earthquake records. For example, under the orange arrow in Fig. 3d the v-shape is questionable. Other effects such as tube waves that occur when the cable is locally sub-vertical due to strong topographic changes may also provoke similar features in the recordings (Daley et al., 2013; Munn et al., 2017). Similarly, basin-edge effects, as observed in the synthetics (Fig. S5b), can also create scattering in the earthquake wavefield and can further complicate such interpretation (blue box in Fig. 3D.

In the eastern region of the cable the S-wave velocity of the shallow sediments is relatively low (∼600 m/s; Fig. 3b), meaning that the wavelengths are lower than 400 m. This is significantly less than the sediment thickness (1100-1400 m), suggesting that a S-wave reverberation could easily occur. In this case, the two phases of opposite polarity observed at ∼4.9 and ∼9.8 s can be seen as a two-way and a four-way travel time reflected S waves. In Fig. 3c, the ∼4.9 s reflection might be still contaminated by the lower frequency surface-wave sides lobes; however, the second reflection at ∼9.8 s is well isolated from any other signal and marks a clear structural interface at depth (yellow box in Fig. 3c) although it has a much lower amplitude. Similar features were also observed to be persistent at OBS stations few hundreds of kilometers away from the Sanriku cable (Tonegawa et al., 2013).

In order to gain confidence in this interpretation, we analyzed an earthquake (M_w=3.1) recorded by station SOB3 with a local incidence angle of ∼7° (Fig. 1). We examined the waveforms after applying the rotation of the 3 components following Nakamura and Hayashimoto (2018) and a lowpass filter at 10 Hz (Fig. 4). On the horizontal component parallel to the cable a clear P to S converted wave appears ∼2.2 s after the P wave. As converted S waves typically happen at the bottom of sedimentary layers, their travel times may be used to quantify the thickness-velocity ratio of such sediment. In this case, a velocity of 600 m/s for a thickness of 1200 m explains the observation which therefore supports our previous interpretation and the inverted velocity model. Unfortunately, no clear P to S conversions were observed with DAS, probably because of its poor sensitivity to sub-perpendicularly incident P-waves.

The inverted shear-wave velocity model and the reflection image suggest that the interface between sedimentary layers and Cretaceous basement is mostly horizontal in the eastern section of the cable from channel ∼6,000–10,000. Considering a vertical reflection at this interface, the horizontal geometry and the strong impedance contrast is favorable toward the retrieval of a sharp signal with displacement data (e.g. Tonegawa et al., 2013). On the other hand, because the strain is the derivative of the displacement ($\epsilon_{xx} = \frac{\partial u_x}{\partial x}$), a reflection between two perfectly parallel horizontal interfaces measured with DAS should be seen as null ($\frac{\partial u_x}{\partial x} = 0$). This may explain the low amplitude of the DAS S-wave reflection signal; however the fact that we observe it implicitly suggests a high level of roughness between the basement and the sedimentary layer. Such roughness at the interface between the sedimentary layers and the Cretaceous bedrock is very well reported by active source reflection profiling data taken at the vicinity of the cable (Geological Survey of Japan, 2013; Minoura et al., 2015; Kodaira et al., 2017). Finally, we acknowledge that another possibility to explain the detection of these somewhat surprising phases could be attributed to incomplete reconstruction of the Green's functions by uneven noise sources distribution. The later may lead to the retrieval of strong amplitude spurious phases on the vertical components (e.g., Boué et al., 2013).

Our final interpretation of the marine shallow geology under the cable is described in Fig. 3e.

4 Conclusions

We demonstrated for the first time that existing fiber-optic cable, otherwise employed for telecommunication between OBS, can also be used to image the properties of the shallow sediments at the bottom of the ocean and so, at a resolution and a spatial extend hardly attainable with traditional active or passive seismic arrays. The only requirement is to connect a DAS interrogator to one end of the cable and record continuous seismic wavefield. As the fiber is a passive component, no other electronic equipment needs to be installed and the fiber can be used for a virtually unlimited amount of time, providing a low-cost instrumentation of the ocean bottom.

As indicated in earlier prototype studies, we confirmed that ocean-bottom DAS is able to record both seismic waves and oceanic waves meaning that a broad range of scientific applications can be explored with such technology. Here, we only used one day of continuous ASF to explore two potential applications of DAS for shallow imaging at the ocean-bottom. First, we extracted multi-mode Scholte-wave dispersion curves from frequency-wavenumber analysis. These dispersion curves were then inverted to provide a 2D profile of the shear-wave velocity. Second, we showed that dynamic strain DAS can provide 2D reflection image using the auto-correlation method. The reflection image high-

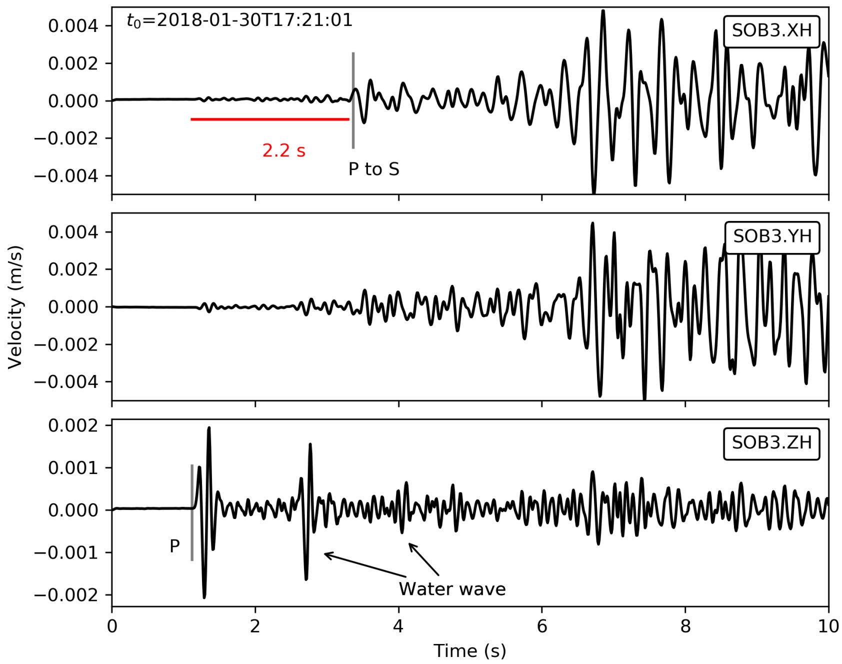

Figure 4: Earthquake recorded by OBS system SOB3 which highlights P to S conversion at the bottom of the sedimentary layer.

lighted a potential two- and four-way travel time S wave reverberating at the bottom of a sedimentary layer, and strong reverberations inside a low velocity micro-basin. These results are supported by the observation of extremely low sediment velocities and high amplitude of Scholte wave in the region, but also by detailed inspection of earthquake wavefield and corresponding modeling. Furthermore, earthquake wavefield analysis allows us to highlight scattering effects associated with fault zones and sedimentary micro basin edges. Combining these techniques, the final interpretation of the marine shallow geology under the cable is sketched in Fig. 3e.

The techniques presented here allowed us to further quantify the properties and geometries of the shallow Neogene marine sediments on top of a Cretaceous basement along 50-km of the fiber cable. Our results open new opportunities for ocean-bottom seismic imaging and exploration that could be performed in the future in a much more cost-effective way.

Acknowledgments

Z.S. and F.P. thank the long-term researcher visiting program of the Earthquake Research Institute of the University of Tokyo. Z.S thanks Mathieu Perton for interesting discussions and Jorjón Castellanos for his help with the calculation of the synthetic seismograms in Fig. S5. T.A. is supported by a JSPS KAKENHI Grant #JP19K21892. We thank Fujitsu Laboratories Ltd. for their collaboration in the field data acquisition. All the figures have been plotted with Matplotlib (Hunter, 2007), and most of the data processing steps have been performed using ObsPy (Beyreuther et al., 2010) and Pyrocko (Heimann et al., 2017). The authors wish to thank the editor, Yunyue Elita Li and an anonymous referee for their review that helped to improve the quality of the paper and the interpretation of the results. **Data and materials availability:** The data useful to reproduce all the figures are available at: https://doi.org/10.5281/zenodo.3928199. Waveforms for Fig. 4 are available for download on the NIED website (https://www.bosai.go.jp/e/).

References

Akal, T. and J. M. Berkson (2013). *Ocean seismo-acoustics: low-Frequency underwater acoustics*, Volume 16. Springer Science & Business Media.

Akuhara, T., M. G. Bostock, A. P. Plourde, and M. Shinohara (2019). Beyond receiver functions: Green's function estimation by transdimensional inversion and its application to obs data. *Journal of Geophysical Research: Solid Earth 124*(2), 1944–1961.

Ardhuin, F., E. Stutzmann, M. Schimmel, and A. Mangeney (2011). Ocean wave sources of seismic noise. *Journal of Geophysical Research: Oceans 116*(C9).

Ayres, A. and F. Theilen (2001). Relationship between P-and S-wave velocities and geological properties of near-surface sediments of the continental slope of the Barents Sea. *Geophysical prospecting 47*(4), 431–441.

Beyreuther, M., R. Barsch, L. Krischer, T. Megies, Y. Behr, and J. Wassermann (2010, May). ObsPy: A Python Toolbox for Seismology. *Seismological Research Letters 81*(3), 530–533.

Boué, P., P. Poli, M. Campillo, H. Pedersen, X. Briand, and P. Roux (2013). Teleseismic correlations of ambient seismic noise for deep global imaging of the earth. *Geophysical Journal International*, ggt160.

Buffoni, C., M. Schimmel, N. C. Sabbione, M. L. Rosa, and G. Connon (2019). Crustal structure beneath Tierra del Fuego, Argentina, inferred from seismic P-wave receiver functions and ambient noise autocorrelations. *Tectonophysics 751*, 41–53.

Cedilnik, G., G. Lees, P. Schmidt, S. Herstrøm, and T. Geisler (2019). Ultra-long reach fiber distributed acoustic sensing for power cable monitoring. In *Proceedings of the JICABLE.*

Claerbout, J. F. (1968). Synthesis of a layered medium from its acoustic transmission response. *Geophysics 33*(2), 264–269.

Clayton, R. W. (2020). Imaging the subsurface with ambient noise autocorrelations. *Seismological Research Letters 91*(2A), 930–935.

Daley, T. M., B. M. Freifeld, J. Ajo-Franklin, S. Dou, R. Pevzner, V. Shulakova, S. Kashikar, D. E. Miller, J. Goetz, J. Henninges, and S. Lueth (2013). Field testing of fiber-optic distributed acoustic sensing (DAS) for subsurface seismic monitoring. *The Leading Edge 32*(6), 699–706.

Geological Survey of Japan (2013). 3.5khz SBP database.

Gill, A. (1982). Ocean-atmosphere dynamics. *International Geophysics Series 30*.

Grattan, K. and T. Sun (2000). Fiber optic sensor technology: an overview. *Sensors and Actuators A: Physical 82*(1-3), 40–61.

Hasselmann, K. (1963). A statistical analysis of the generation of microseisms. *Reviews of Geophysics 1*(2), 177–210.

Heimann, S., M. Kriegerowski, M. Isken, S. Cesca, S. Daout, F. Grigoli, C. Juretzek, T. Megies, N. Nooshiri, A. Steinberg, et al. (2017). Pyrocko - An open-source seismology toolbox and library. *GFZ Data Services*.

Herrmann, R. B. (1996). Computer proramms in seismology.

Hunter, J. D. (2007, May). Matplotlib: A 2D Graphics Environment. *Computing in Science and Engineering 9*(3), 90–95.

Kanazawa, T. and A. Hasegawa (1997). Ocean-bottom observatory for earthquakes and tsunami off Sanriku, north-east Japan using submarine cable, paper presented at international workshop on scientific use of submarine cables, comm. for sci. *Use of Submarine Cables, Okinawa, Japan*.

Kanazawa, T., W. Sager, C. Escutia, et al. (2001). Proc. odp, init. repts., 191, college station, tx (ocean drilling program).

Kanazawa, T., K. Uehira, M. Mochizuki, T. Shinbo, H. Fujimoto, S. Noguchi, T. Kunugi, K. Shiomi, S. Aoi, T. Matsumoto, and S. Sekiguchi (2016). S-net project, cabled observation network for earthquakes and tsunamis. *Abstract WE2B–3, Presented at SubOptic 2016*, 18–21.

Kennett, B., E. Saygin, and M. Salmon (2015). Stacking autocorrelograms to map Moho depth with high spatial resolution in southeastern Australia. *Geophysical Research Letters 42*(18), 7490–7497.

Kodaira, S., Y. Nakamura, Y. Yamamoto, K. Obana, G. Fujie, T. No, Y. Kaiho, T. Sato, and S. Miura (2017). Depth-varying structural characters in the rupture zone of the 2011 Tohoku-oki earthquake. *Geosphere 13*(5), 1408–1424.

Koketsu, K., H. Miyake, and H. Suzuki (2012). Japan integrated velocity structure model version 1. In *Proceedings of the 15th World Conference on Earthquake Engineering*, Number 1773. Lisbon.

Kugler, S., T. Bohlen, T. Forbriger, S. Bussat, and G. Klein (2007). Scholte-wave tomography for shallow-water marine sediments. *Geophysical Journal Interna-*

tional 168(2), 551–570.

Li, D., D. Helmberger, R. W. Clayton, and D. Sun (2014). Global synthetic seismograms using a 2-d finite-difference method. *Geophysical Journal International 197*(2), 1166–1183.

Lindsey, N. J., T. C. Dawe, and J. B. Ajo-Franklin (2019). Illuminating seafloor faults and ocean dynamics with dark fiber distributed acoustic sensing. *Science 366*(6469), 1103–1107.

Longuet-Higgins, M. S. (1950). A theory of the origin of microseisms. *Philosophical Transactions of the Royal Society of London A: Mathematical, Physical and Engineering Sciences 243*(857), 1–35.

Martin, E. R., N. Lindsey, J. Ajo-Franklin, and B. Biondi (2018). Introduction to interferometry of fiber optic strain measurements. *EarthArXiv*.

Minoura, K., D. Sugawara, T. Yamanoi, and T. Yamada (2015). Aftereffects of subduction-zone earthquakes: potential tsunami hazards along the Japan sea coast. *The Tohoku journal of experimental medicine 237*(2), 91–102.

Miyazawa, M., R. Snieder, and A. Venkataraman (2008). Application of seismic interferometry to extract P-and S-wave propagation and observation of shear-wave splitting from noise data at Cold Lake, Alberta, Canada. *Geophysics 73*(4), D35–D40.

Mordret, A., M. Landès, N. Shapiro, S. Singh, and P. Roux (2014). Ambient noise surface wave tomography to determine the shallow shear velocity structure at valhall: depth inversion with a neighbourhood algorithm. *Geophysical Journal International 198*(3), 1514–1525.

Mordret, A., M. Landès, N. M. Shapiro, S. C. Singh, P. Roux, and O. I. Barkved (2013, March). Near-surface study at the Valhall oil field from ambient noise surface wave tomography. *Geophysical Journal International*, ggt061.

Munn, J. D., T. I. Coleman, B. L. Parker, M. J. Mondanos, and A. Chalari (2017). Novel cable coupling technique for improved shallow distributed acoustic sensor vsps. *Journal of Applied Geophysics 138*, 72–79.

Muyzert, E. (2000). Scholte wave velocity inversion for a near surface S-velocity model and PS-statics. In *SEG Technical Program Expanded Abstracts 2000*, pp. 1197–1200. Society of Exploration Geophysicists.

Nakamura, T. and N. Hayashimoto (2018). Rotation motions of cabled ocean-bottom seismic stations during the 2011 Tohoku earthquake and their effects on magnitude estimation for early warnings. *Geophysical Journal International 216*(2), 1413–1427.

Nakamura, Y., S. Kodaira, B. J. Cook, T. Jeppson, T. Kasaya, Y. Yamamoto, Y. Hashimoto, M. Yamaguchi, K. Obana, and G. Fujie (2014). Seismic imaging and velocity structure around the JFAST drill site in the Japan Trench: low Vp, high Vp/Vs in the transparent frontal prism. *Earth, Planets and Space 66*(1), 121.

Nolet, G. and L. M. Dorman (1996). Waveform analysis of Scholte modes in ocean sediment layers. *Geophysical Journal International 125*(2), 385–396.

Oren, C. and R. L. Nowack (2016). Seismic body-wave interferometry using noise auto-correlations for crustal structure. *Geophysical Journal International*, ggw394.

Perton, M., Z. Spica, and C. Caudron (2017). Inversion of the horizontal-to-vertical spectral ratio in presence of strong lateral heterogeneity. *Geophysical journal international 212*(2), 930–941.

Phạm, T. and H. Tkalčić (2017). On the feasibility and use of teleseismic P wave coda autocorrelation for mapping shallow seismic discontinuities. *Journal of Geophysical Research: Solid Earth 122*(5), 3776–3791

Posey Jr., R., G. A. Johnson, and S. T. Vohra (2000). Strain sensing based on coherent Rayleigh scattering in an optical fibre. *Electronics Letters 36*(20), 1.

Ritzwoller, M. H. and A. L. Levshin (2002). Estimating shallow shear velocities with marine multicomponent seismic data. *Geophysics 67*(6), 1991–2004.

Romero, P. and M. Schimmel (2018). Mapping the basement of the ebro basin in spain with seismic ambient noise autocorrelations. *Journal of Geophysical Research: Solid Earth 123*(6), 5052–5067.

Ruigrok, E. and K. Wapenaar (2012). Global-phase seismic interferometry unveils P-wave reflectivity below the Himalayas and Tibet. *Geophysical Research Letters 39*(11).

Sanchez-Sesma, F. J. (1987). Site effects on strong ground motion. *Soil Dynamics and Earthquake Engineering 6*(2), 124–132.

Saygin, E., P. R. Cummins, and D. Lumley (2017). Retrieval of the P wave reflectivity response from autocorrelation of seismic noise: Jakarta Basin, Indonesia. *Geophysical Research Letters 44*(2), 792–799.

Schalkwijk, K., C. Wapenaar, and D. Verschuur (2000). Decomposition of multi-component ocean-bottom data: inversion for the sub-bottom parameters. In *SEG Technical Program Expanded Abstracts 2000*, pp. 1205–1208. Society of Exploration Geophysicists.

Schimmel, M. and H. Paulssen (1997). Noise reduction and detection of weak, coherent signals through phase-weighted stacks. *Geophysical Journal International 130*(2), 497–505.

Scholte, J. G. J. (1958). Rayleigh waves in isotropic and anistropic elastic media. *Meded. Verhand. KNMI 72*, 9–43.

Shinohara, M., T. Fukano, T. Kanazawa, E. Araki, K. Suyehiro, M. Mochizuki, K. Nakahigashi, T. Yamada, and K. Mochizuki (2008). Upper mantle and crustal seismic structure beneath the Northwestern Pacific Basin using a seafloor borehole broadband seismometer and ocean bottom seismometers. *Physics of the Earth and Planetary Interiors 170*(1-2), 95–106.

Shinohara, M., Y. Machida, T. Yamada, K. Nakahigashi, T. Shinbo, K. Mochizuki, Y. Murai, R. Hino, Y. Ito, T. Sato, et al. (2012). Precise aftershock distribution of the 2011 off the Pacific coast of Tohoku earthquake revealed by an ocean-bottom seismometer network. *Earth, planets and space 64*(12), 8.

Shinohara, M., T. Yamada, T. Akuhara, K. Mochizuki, S. Sakai, M. Hamakawa, T. Kasajima, T. Arioka, and S. Kubota (2019). Distributed acoustic sensing measurement by using seafloor optical fiber cable system off Sanriku for seismic observation. In *OCEANS 2019 MTS/IEEE SEATTLE*, pp. 1–4. IEEE.

Shinohara, M., T. Yamada, S. Sakai, H. Shiobara, and T. Kanazawa (2016). Development and installation of new seafloor cabled seismic and tsunami observation system using ICT. In *OCEANS 2016 MTS/IEEE Monterey*, pp. 1–4. IEEE.

Sladen, A., D. Rivet, J.-P. Ampuero, L. De Barros, Y. Hello, G. Calbris, and P. Lamare (2019). Distributed sensing of earthquakes and ocean-solid earth interactions on seafloor telecom cables. *Nature Communications 10*(1), 1–8.

Socco, V. L., D. Boiero, M. Maraschini, M. Vanneste, C. Madshus, H. Westerdahl, K. Duffaut, and E. Skomedal (2011). On the use of the Norwegian Geotechnical institute's prototype seabed-coupled shear wave vibrator for shallow soil characterization-II. Joint inversion of multimodal Love and Scholte surface waves. *Geophysical Journal International 185*(1), 237–252.

Spica, Z., D. Legrand, A. Iglesias, T. R. Walter, H. Sebastian, T. Dahm, J.-L. Froger, D. Rémy, S. Bonvalot, and M. Pardo (2015). Hydrothermal and magmatic reservoirs at Lazufre volcanic area, revealed by a high-resolution seismic noise tomography. *Earth and Planetary Science Letters 421*, 27–38.

Spica, Z. J., M. Perton, N. Nakata, X. Liu, and G. C. Beroza (2017). Site characterization at Groningen gas field area through joint surface-borehole H/V analysis. *Geophysical Journal International 212*(1), 412–421.

Sun, W. and B. Kennett (2016). Receiver structure from teleseisms: Autocorrelation and cross correlation. *Geophysical Research Letters 43*(12), 6234–6242.

Suzuki, W., S. Aoi, H. Sekiguchi, and T. Kunugi (2011). Rupture process of the 2011 Tohoku-Oki mega-thrust earthquake (M9. 0) inverted from strong-motion data. *Geophysical Research Letters 38*(7).

Taylor, G., S. Rost, and G. Houseman (2016). Crustal imaging across the North Anatolian Fault Zone from the autocorrelation of ambient seismic noise. *Geophysical Research Letters 43*(6), 2502–2509.

Tonegawa, T., Y. Fukao, K. Nishida, H. Sugioka, and A. Ito (2013). A temporal change of shear wave anisotropy within the marine sedimentary layer associated with the 2011 Tohoku-Oki earthquake. *Journal of Geophysical Research: Solid Earth 118*(2), 607–615.

Vardy, M. E., M. Vanneste, T. J. Henstock, M. A. Clare, C. F. Forsberg, and G. Provenzano (2017). State-of-the-art remote characterization of shallow marine sediments: the road to a fully integrated solution. *Near Surface Geophysics 15*(4), 387–402.

Williams, E. F., M. R. Fernández-Ruiz, R. Magalhaes, R. Vanthillo, Z. Zhan, M. González-Herráez, and H. F. Martins (2019). Distributed sensing of microseisms and teleseisms with submarine dark fibers. *Nature communications 10*(1), 1–11.

Yao, H., P. Gouedard, J. A. Collins, J. J. McGuire, and R. D. van der Hilst (2011). Structure of young East Pacific Rise lithosphere from ambient noise correlation analysis of fundamental-and higher-mode Scholte-Rayleigh waves. *Comptes Rendus Geoscience 343*(8-9), 571–583.

Figure 1.

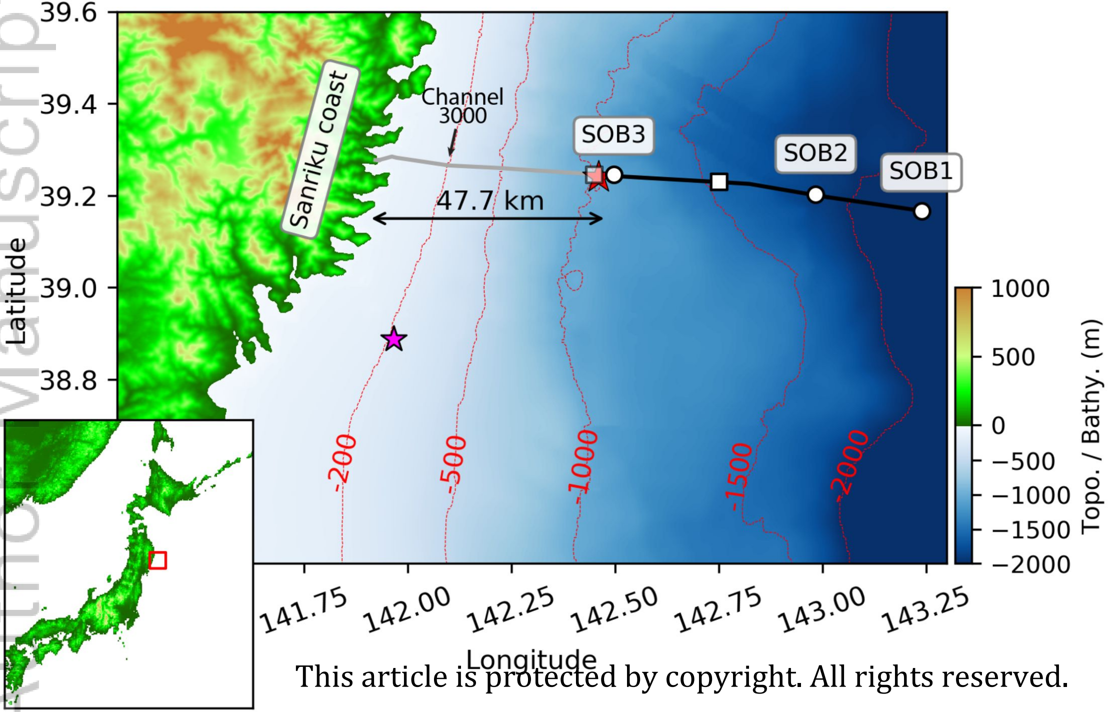

39.6
39.4
39.2
39.0
38.8
Latitude
Sanriku coast
Channel 3000
SOB3
SOB2
SOB1
47.7 km
-200
-500
-1000
-1500
-2000
141.75
142.00
142.25
142.50
142.75
143.00
143.25
Longitude
1000
500
0
−500
−1000
−1500
−2000
Topo. / Bathy. (m)

Figure 2.

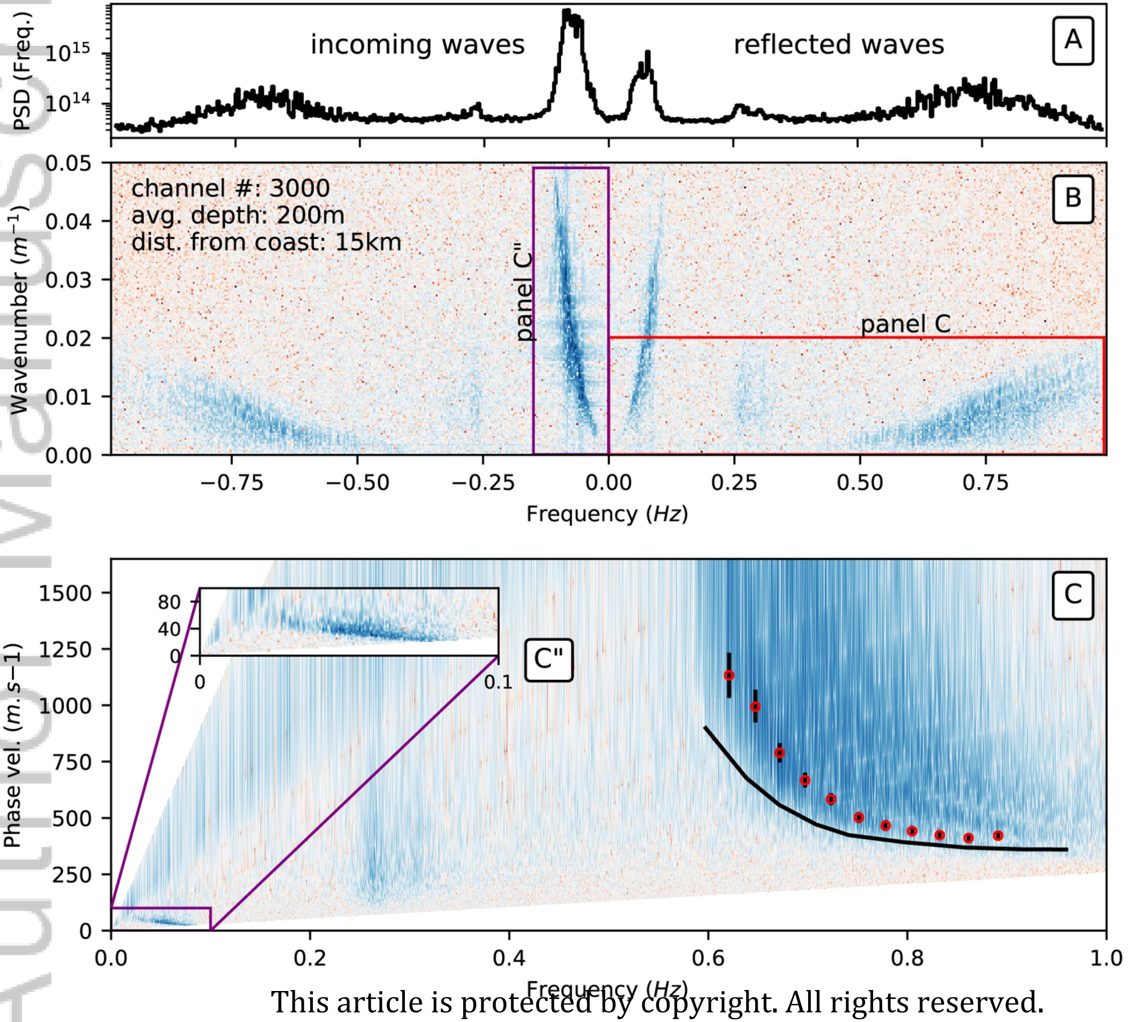
PSD (Freq.)
10^{15}
10^{14}
incoming waves
reflected waves
A
B
channel #: 3000
avg. depth: 200m
dist. from coast: 15km
panel C"
panel C
Wavenumber (m^{-1})
0.05
0.04
0.03
0.02
0.01
0.00
−0.75
−0.50
−0.25
0.00
0.25
0.50
0.75
Frequency (Hz)
C
C"
Phase vel. (m.s−1)
1500
1250
1000
750
500
250
0
80
40
0
0
0.1
0.0
0.2
0.4
0.6
0.8
1.0
Frequency (Hz)

Figure 3.

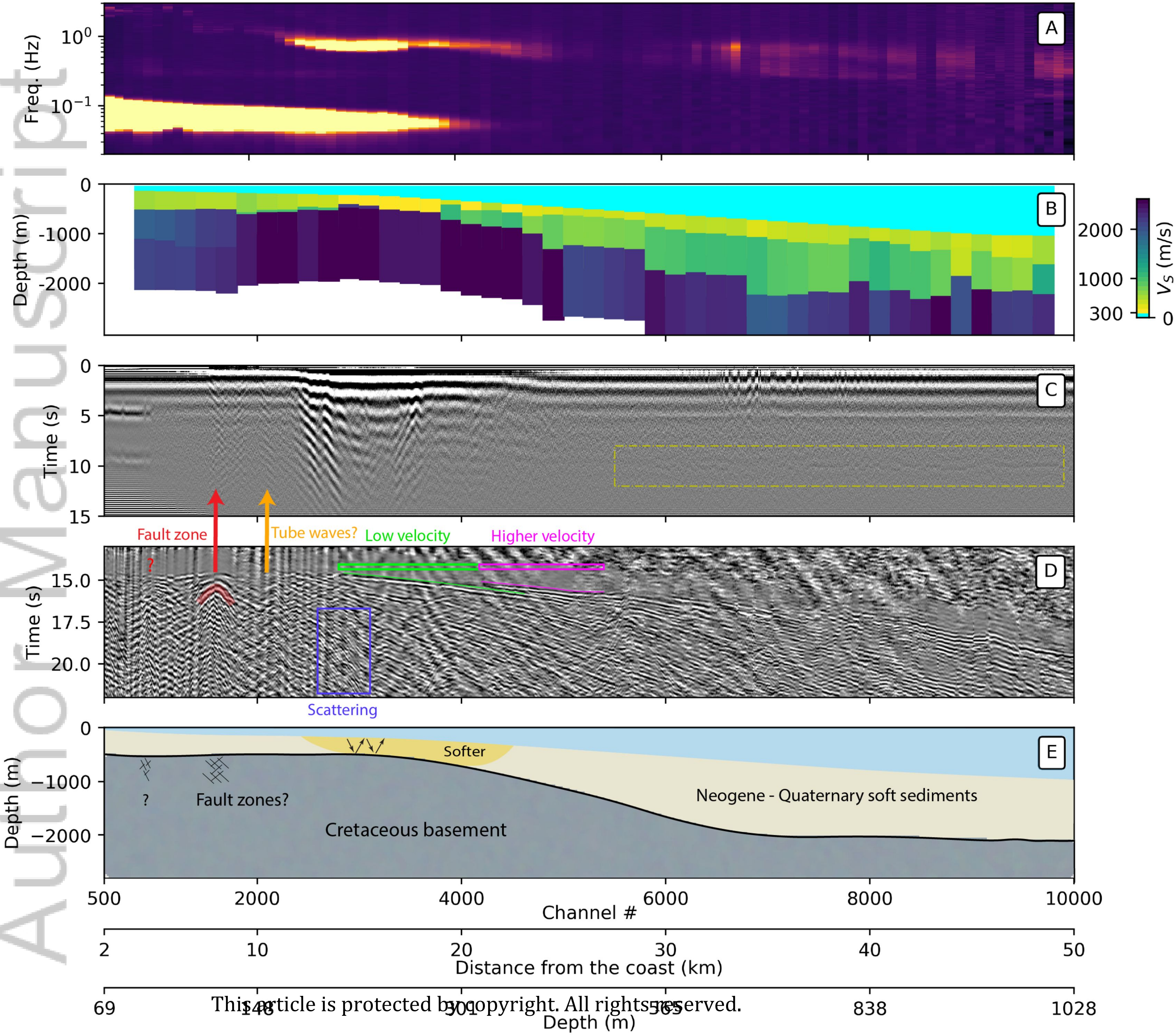
A
B
C
D
E
Freq. (Hz)
10^0
10^{-1}
Depth (m)
0
-1000
-2000
V_S (m/s)
2000
1000
300
0
Time (s)
5
10
15
Fault zone
Tube waves?
Low velocity
Higher velocity
?
15.0
17.5
20.0
Scattering
Softer
Fault zones?
Cretaceous basement
Neogene - Quaternary soft sediments
500
2000
4000
6000
8000
10000
Channel #
2
10
20
30
40
50
Distance from the coast (km)
69
148
301
565
838
1028
Depth (m)

Figure 4.

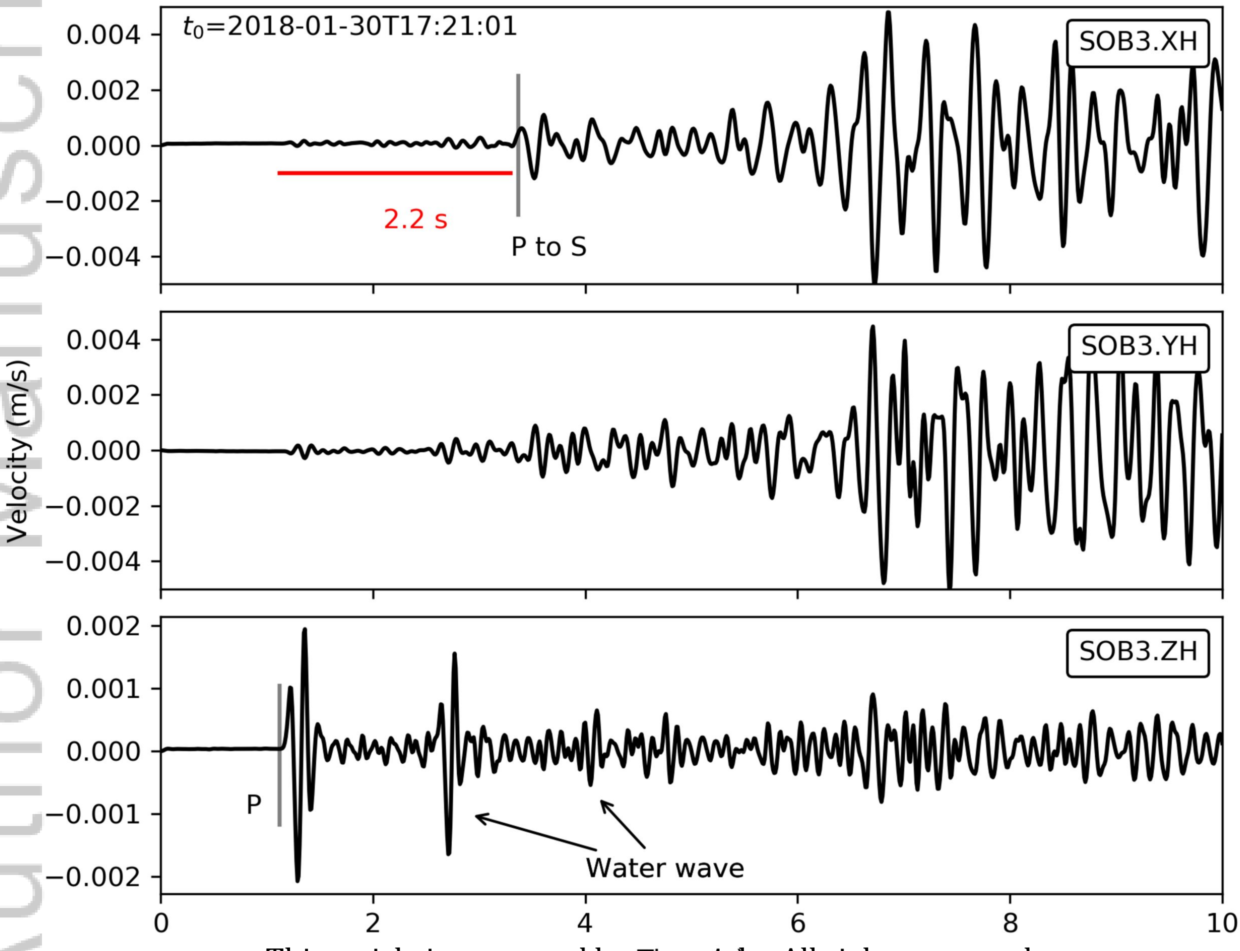

t_0=2018-01-30T17:21:01
SOB3.XH
2.2 s
P to S
SOB3.YH
SOB3.ZH
P
Water wave
Velocity (m/s)
Time (s)
0.004
0.002
0.000
−0.002
−0.004
0.001
−0.001
0
2
4
6
8
10

Figure S1.

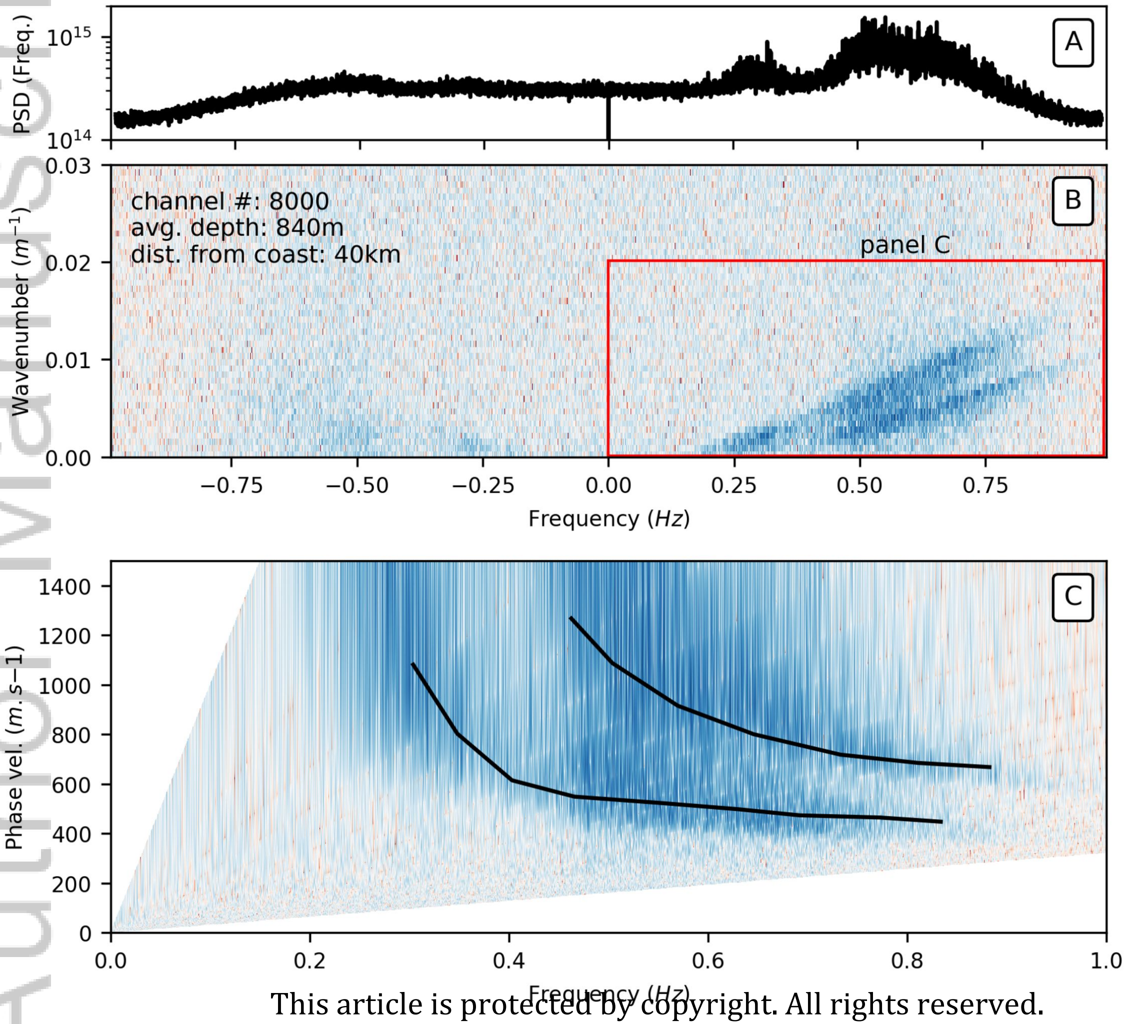
A
PSD (Freq.)
10^{15}
10^{14}
B
channel #: 8000
avg. depth: 840m
dist. from coast: 40km
panel C
Wavenumber (m^{-1})
0.03
0.02
0.01
0.00
−0.75
−0.50
−0.25
0.00
0.25
0.50
0.75
Frequency (Hz)
C
Phase vel. ($m.s-1$)
1400
1200
1000
800
600
400
200
0
0.0
0.2
0.4
0.6
0.8
1.0
Frequency (Hz)

Figure S2.

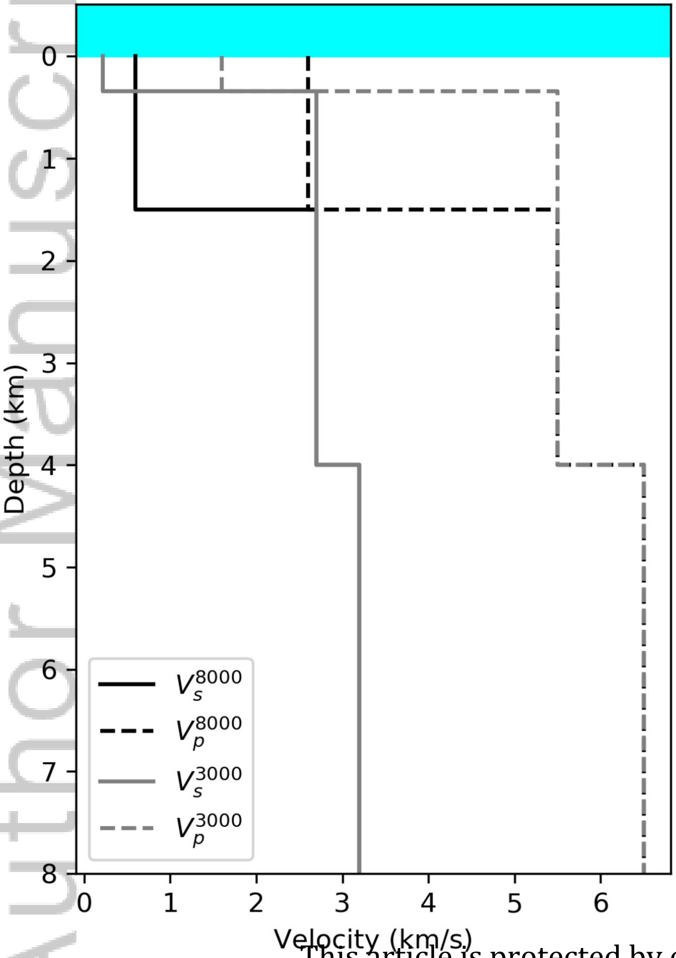

0
1
2
3
4
5
6
7
8
Depth (km)
0
1
2
3
4
5
6
Velocity (km/s)
V_s^{8000}
V_p^{8000}
V_s^{3000}
V_p^{3000}

Figure S3.

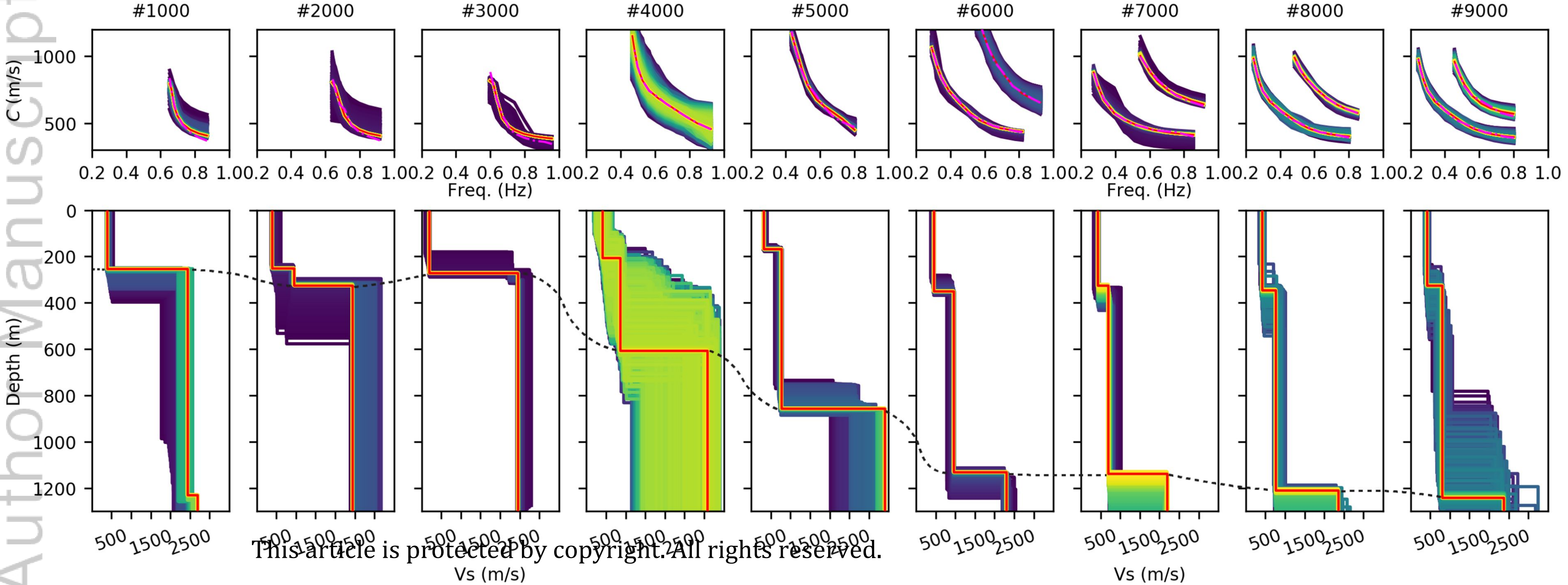

#1000
#2000
#3000
#4000
#5000
#6000
#7000
#8000
#9000
C (m/s)
1000
500
0.2 0.4 0.6 0.8 1.0
Freq. (Hz)
Depth (m)
0
200
400
600
800
1000
1200
500 1500 2500
Vs (m/s)

Figure S4.

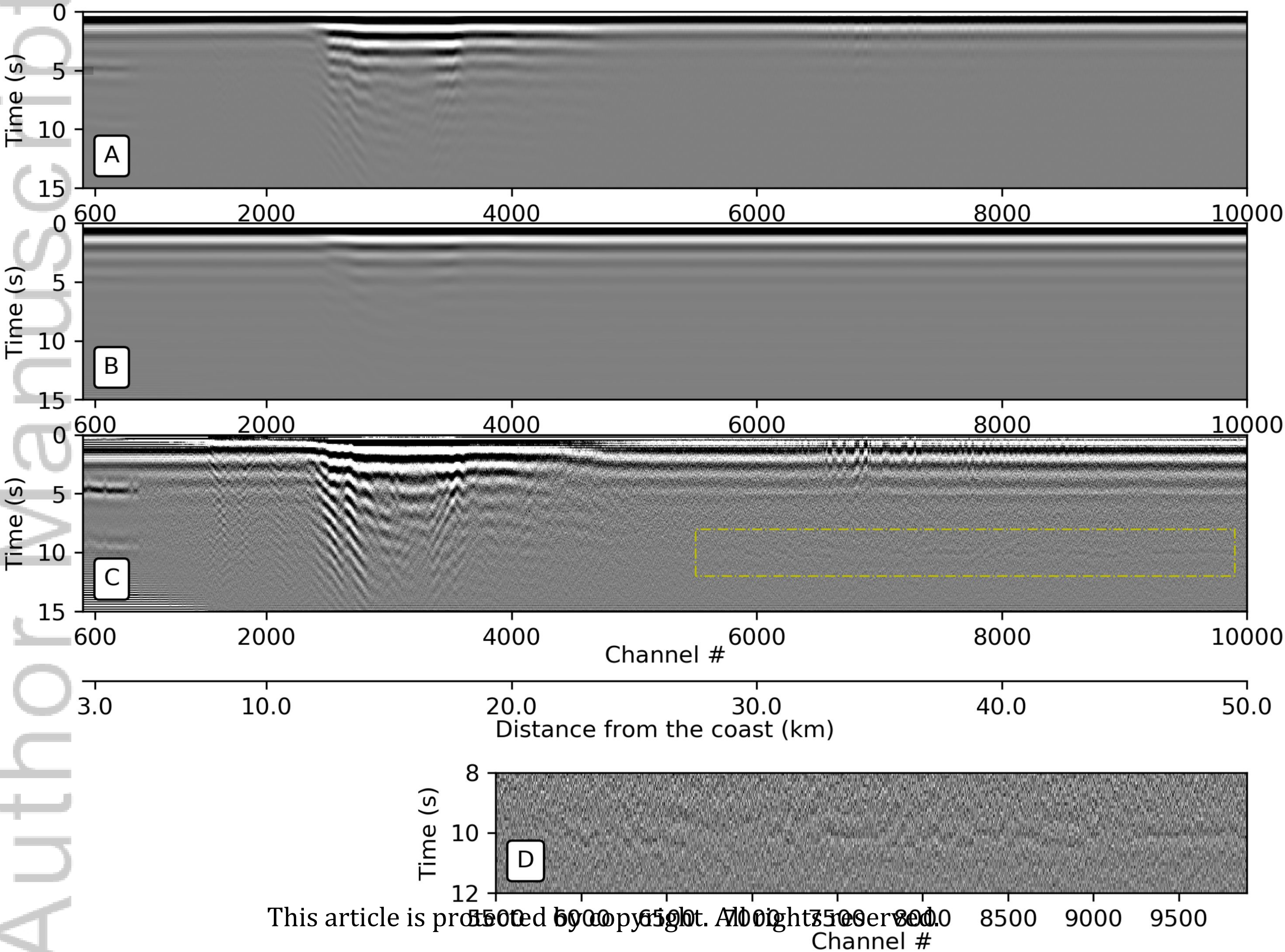

Time (s)
A
B
C
D
Channel #
Distance from the coast (km)

Figure S5.

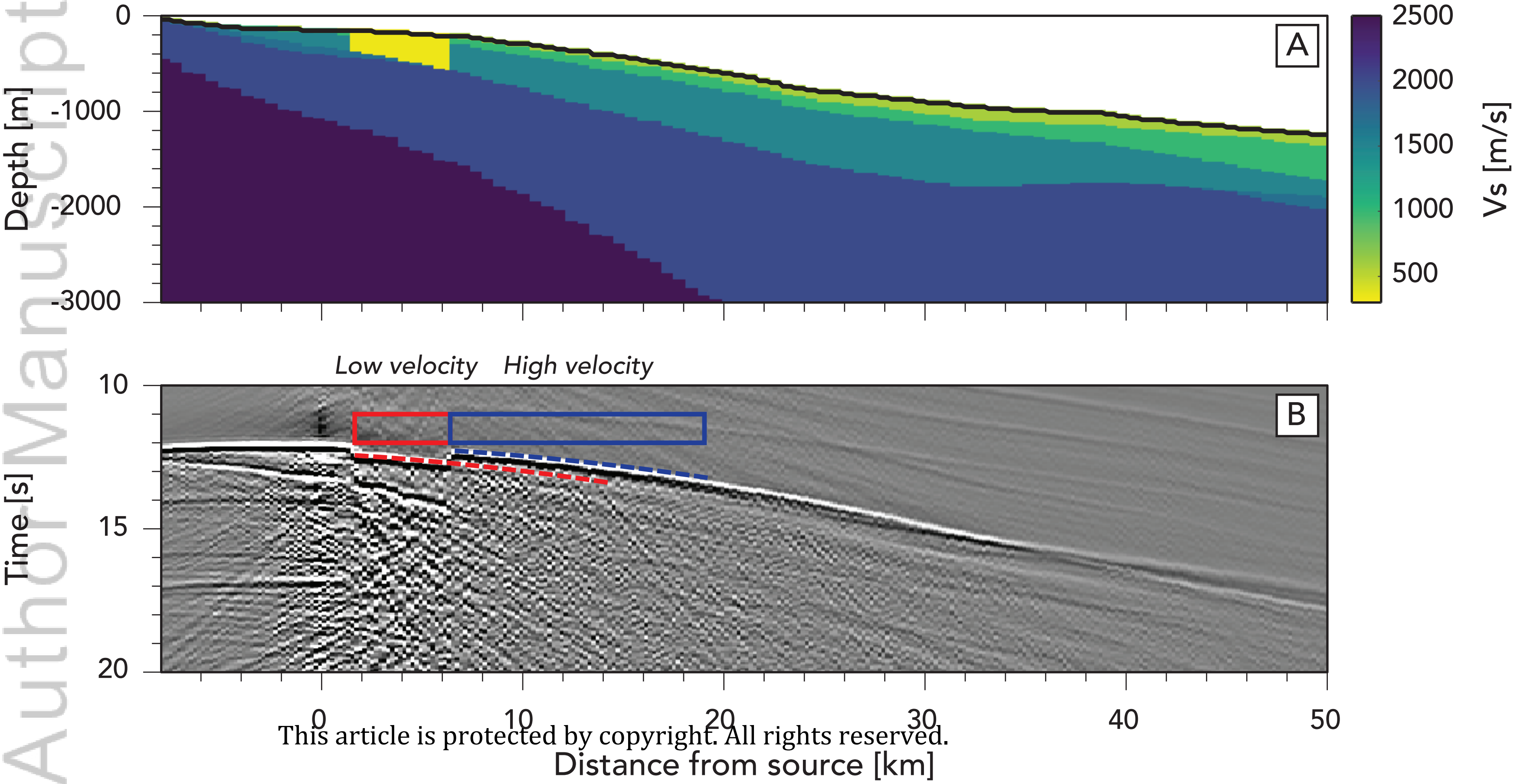

A
B
Depth [m]
0
-1000
-2000
-3000
2500
2000
1500
1000
500
Vs [m/s]
Low velocity
High velocity
Time [s]
10
15
20
0
10
20
30
40
50
Distance from source [km]

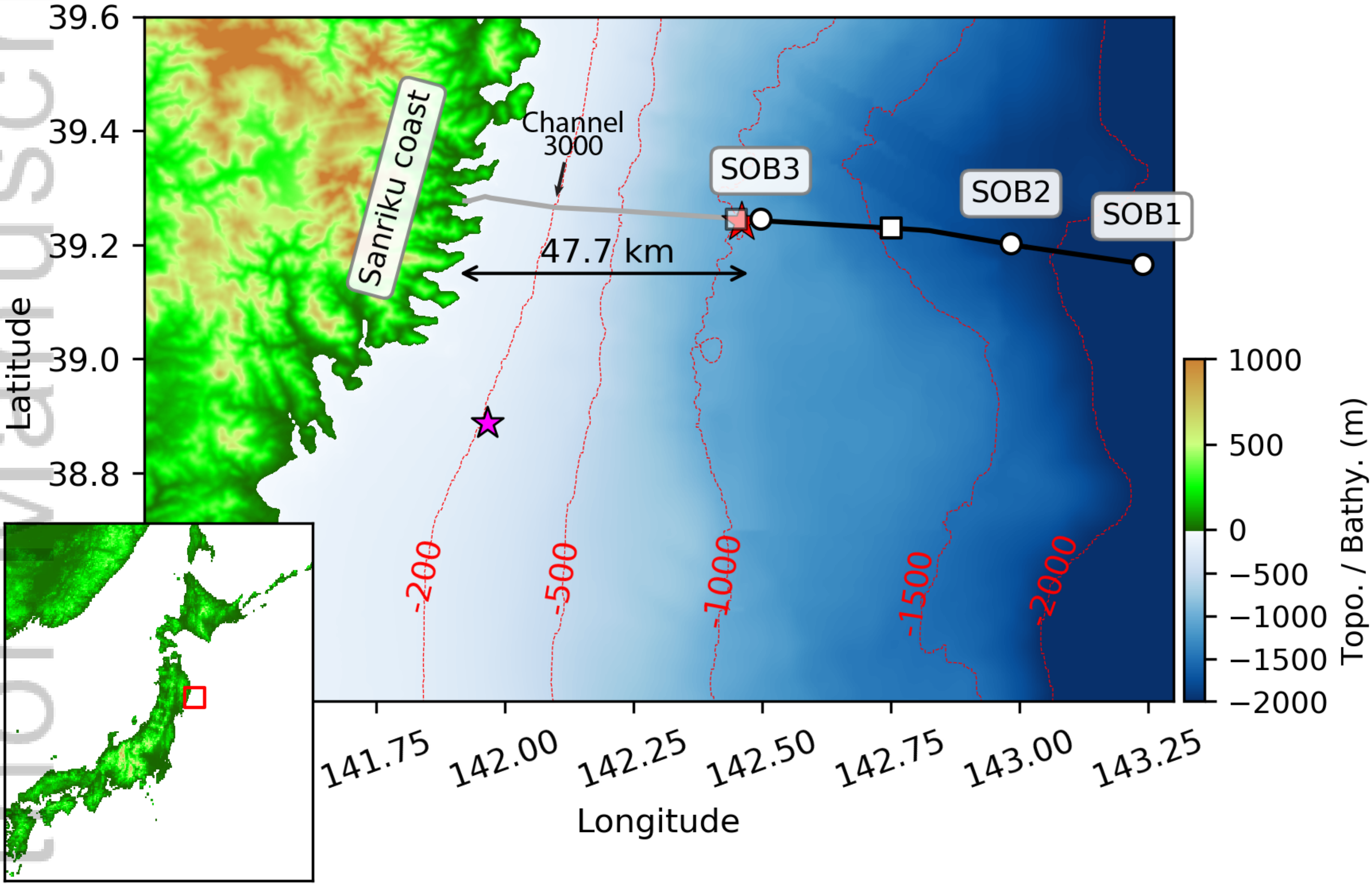

GRL_61098_2020GL088360-f01-z-.png

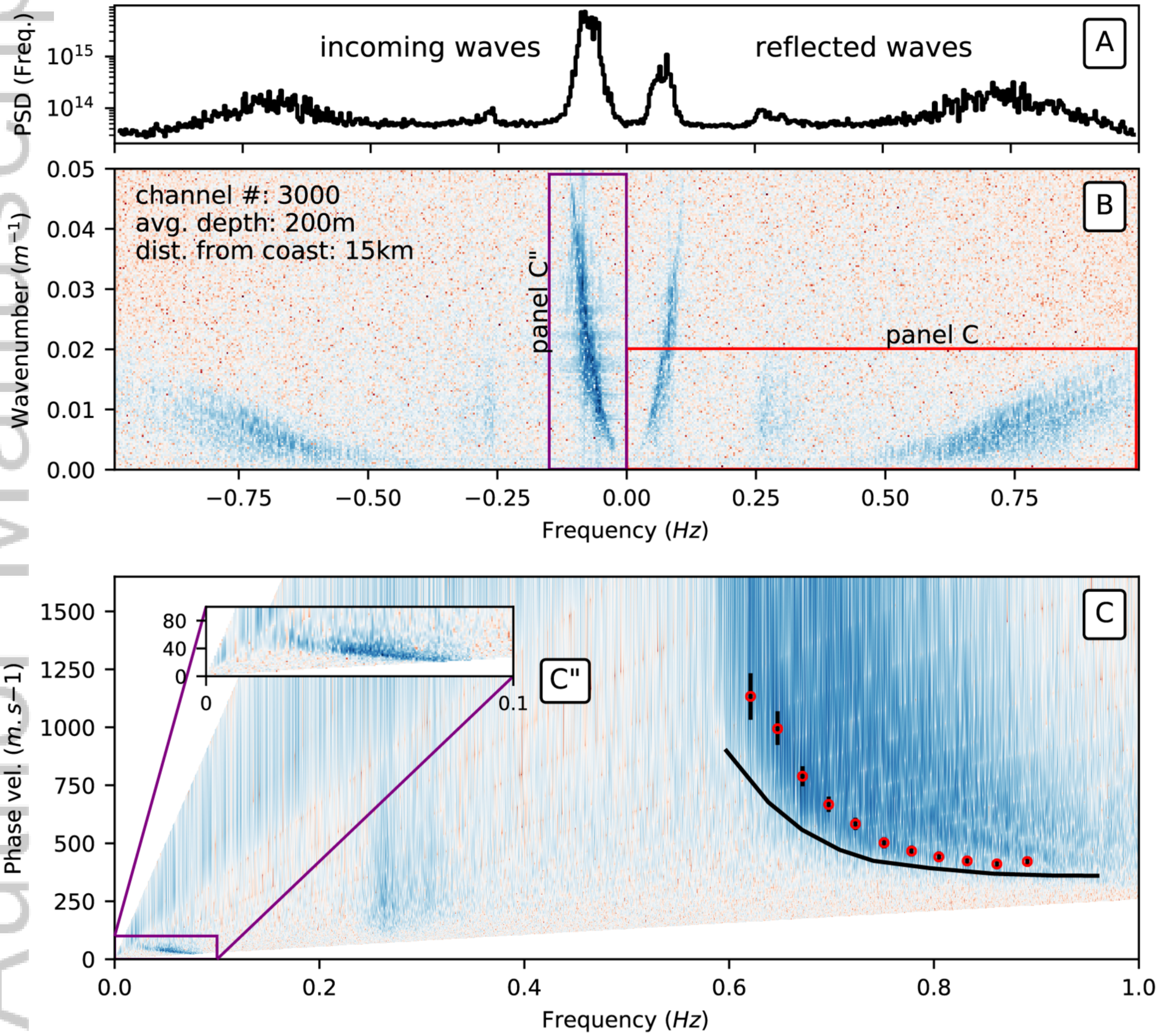

GRL_61098_2020GL088360-f02-z-.png

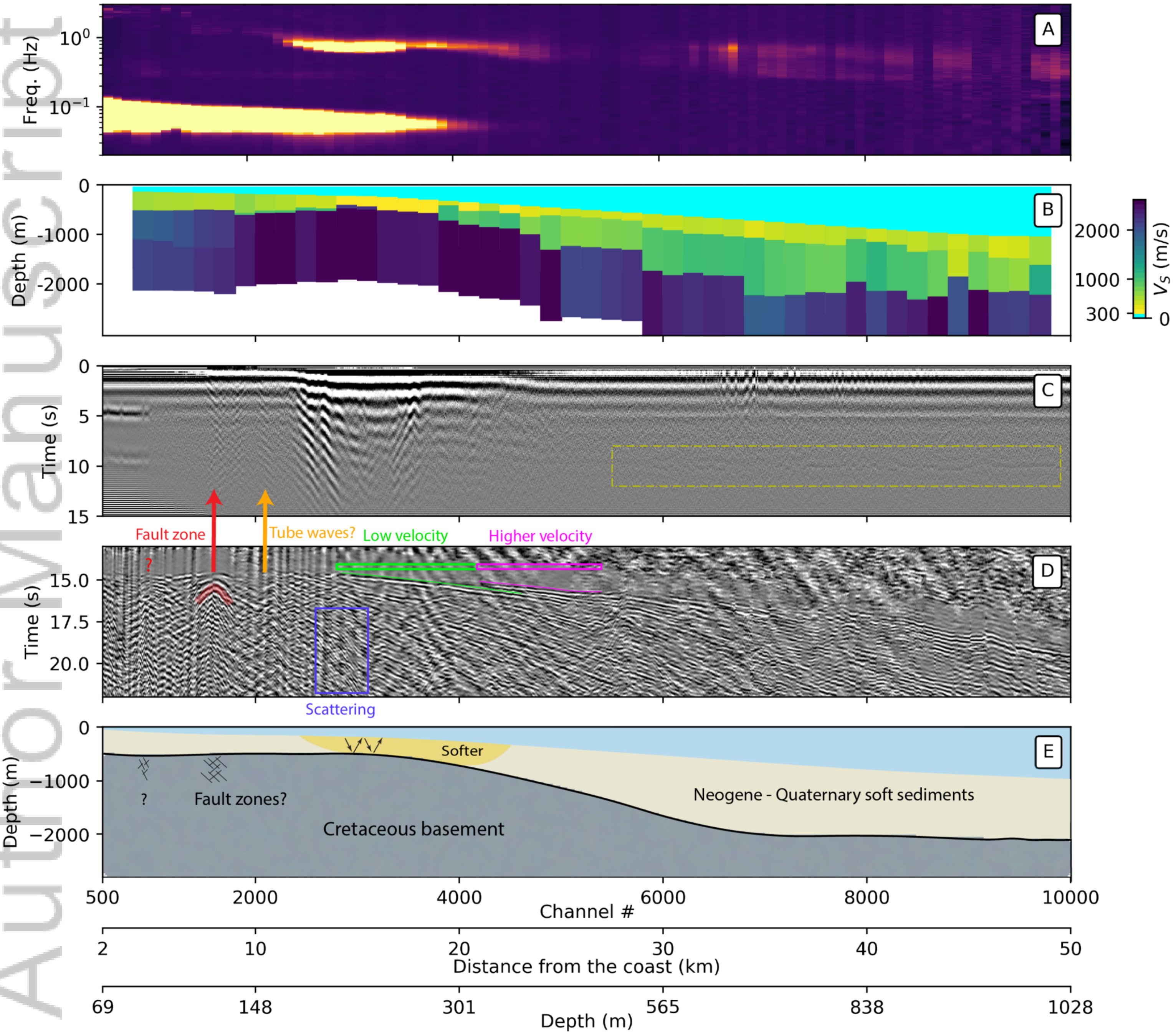

GRL_61098_2020GL088360-f03-z-.png

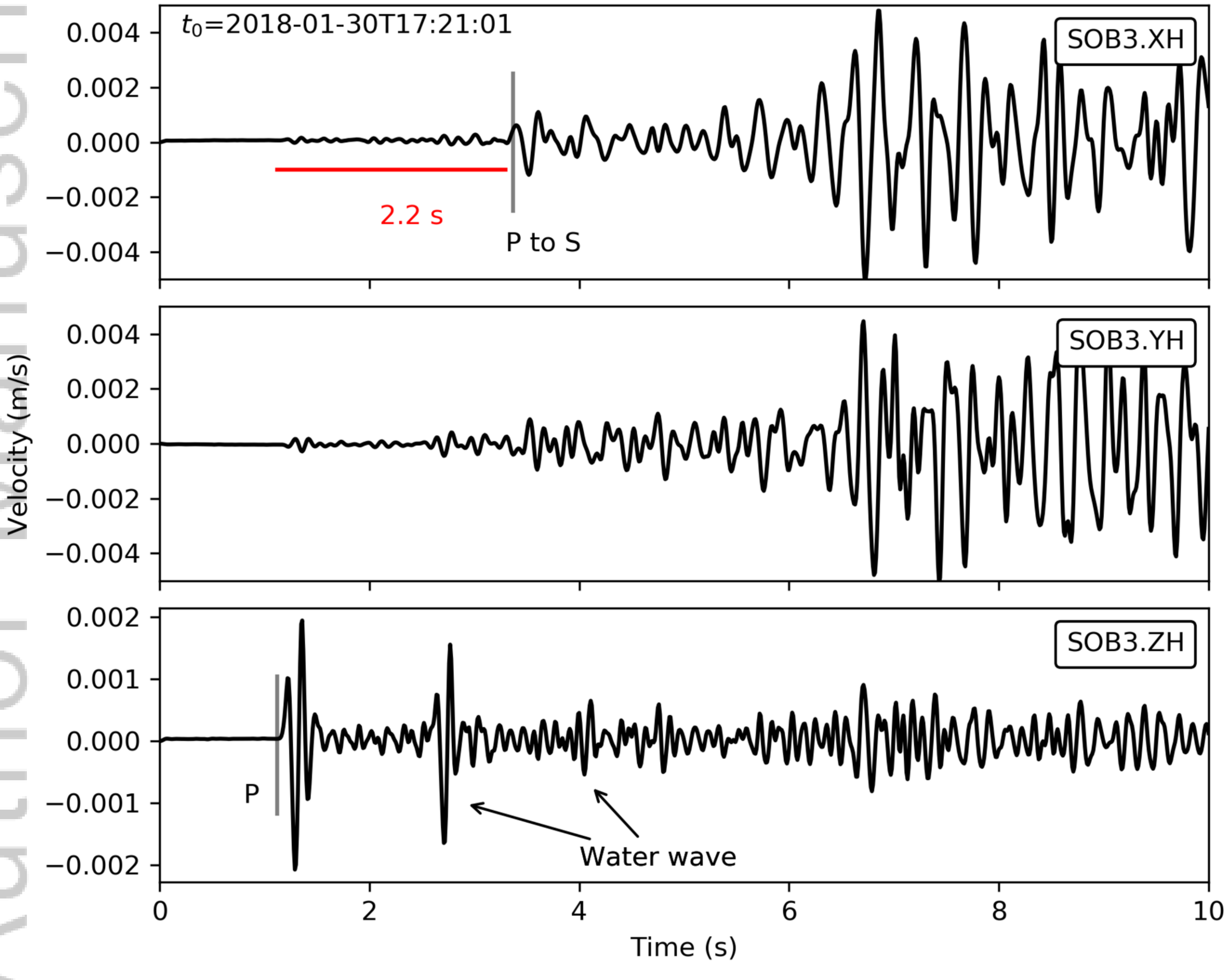

GRL_61098_2020GL088360-f04-z-.png